PAPER

Granular metals with SiN_x dielectrics

To cite this article: Simeon J Gilbert *et al* 2023 *Nanotechnology* **34** 415706

IOP Publishing Nanotechnology
Nanotechnology 34 (2023) 415706 (8pp) https://doi.org/10.1088/1361-6528/ace4d2

Granular metals with SiN_x dielectrics

Simeon J Gilbert*, Melissa L Meyerson, Paul G Kotula, Samantha G Rosenberg, Thomas G Kmieciak, Michael P McGarry, Michael P Siegal and Laura B Biedermann*

Sandia National Laboratories, Albuquerque, NM 87185, United States of America

E-mail: sjgilbe@sandia.gov and lbieder@sandia.gov

Received 25 March 2023, revised 20 June 2023
Accepted for publication 6 July 2023
Published 28 July 2023

Abstract

Understanding and controlling nanoscale interface phenomena, such as band bending and secondary phase formation, is crucial for electronic device optimization. In granular metal (GM) studies, where metal nanoparticles are embedded in an insulating matrix, the importance of interface phenomena is frequently neglected. We demonstrate that GMs can serve as an exemplar system for evaluating the role of secondary phases at interfaces through a combination of x-ray photoemission spectroscopy (XPS) and electrical transport studies. We investigated SiN_x as an alternative to more commonly used oxide-insulators, as SiN_x-based GMs may enable high temperature applications when paired with refractory metals. Comparing Co-SiN_x and Mo-SiN_x GMs, we found that, in the tunneling-dominated insulating regime, Mo-SiN_x had reduced metal-silicide formation and orders-of-magnitude lower conductivity. XPS measurements indicate that metal-silicide and metal-nitride formation are mitigatable concerns in Mo-SiN_x. Given the metal-oxide formation seen in other GMs, SiN_x is an appealing alternative for metals that readily oxidize. Furthermore, SiN_x provides a path to metal-nitride nanostructures, potentially useful for various applications in plasmonics, optics, and sensing.

Supplementary material for this article is available online

Keywords: granular metals, interface phenomena, XPS, STEM, electron tunneling

(Some figures may appear in colour only in the online journal)

Introduction

Granular metals (GMs) consist of distinct metallic and insulating regions; the properties depend on the experimentally-controlled volumetric metal fraction (φ). At high φ (>0.6), GMs are disordered metals with limited insulator inclusions. At low φ (<0.3), the metallic regions exist as isolated metal nanoparticles, and conduction occurs via thermally-assisted electron tunneling and capacitive transport [1–3]. The percolation threshold (φ_c) is the metal fraction where the GM's electronic nature switches from insulating to metallic, and occurs in the $\varphi = 0.3$–0.6 range. Below φ_c, the room temperature DC conduction is dominated by thermally-assisted electron tunneling, which depends on the prevalence of insulator defects and the separation distance between metal nanoparticles [4, 5]. The capacitive transport dominates at high frequencies and scales according to Jonscher's universal power law [6, 7] as confirmed by experiments [8, 9]. We note that at low temperatures GMs also exhibit Coulomb blockade effects, which suppress the current at low voltages [10, 11]. However, here we focus on room temperature conduction where the thermal activation energy is greater than necessary to transfer an electron between adjacent neutral nanoparticles and Coulomb blockade effects are negligible [10].

GMs have been studied for >50 years [12, 13] for both fundamental and applied research in nanoelectronics [14], plasmonics [15], superconductivity [16], and magnetism [17]. While GMs with various metals have been investigated, nearly all GM studies employed oxide-based insulators, such as SiO_2, Al_2O_3, or yttria-stabilized zirconia (YSZ), with notable non-oxides including MgF_2 [18], BN [19], and carbon-based [20, 21] GMs. Recently, we found that GMs with non-noble metals and oxide insulators form metal-oxides, which deleteriously increase GM conductivity at $\varphi < \varphi_c$ [5]. Annealing of GMs causes nanoparticle coalescence and substantially alters the GM electrical properties [2]; high

* Authors to whom any correspondence should be addressed.

thermal stability transition metal-based GMs will enable applications at elevated temperatures and high current densities.

When GMs contain pristine insulators and metallic nanoparticles, without interdiffusion of metallic and insulating species, the conductivity (σ) will approach that of thin metallic films, $\sigma = 10^4$–10^6 S cm^{-1} [4], as φ approaches 1. Below φ_c, the DC conductivity will be dominated by tunneling between the metal nanoparticles and minimally mediated by insulator defects. To evaluate the insulator quality, we consider GM compositions at $\varphi = 0.2$, well within the insulating regime. To date, the GMs with the lowest conductivities all contained Au and Ag nanoparticles, which are resistant to oxidation, and these high-quality GMs can exhibit $\sigma = 10^{-4}$–10^{-6} S cm^{-1} at $\varphi = 0.2$ [4, 5, 13, 22, 23]. For non-noble metals, the metal nanoparticles absorb oxygen from the insulator. The resulting vacancies facilitate conduction through the insulator, thus σ at $\varphi = 0.2$ is 2–4 orders of magnitude higher for non-noble transition metals compared to Au or Ag [5].

To improve the insulating quality of GMs with high thermal stability transition metals, alternative non-oxide insulators may minimize the deleterious secondary phase formations, such as metal-oxides, caused by the interdiffusion of metal and insulator species. We investigated silicon nitride, frequently used as a passivation layer for power electronics, due to its high chemical stability [24–26]. Mo and Co were chosen for direct comparison to Mo-YSZ and Co-YSZ GMs [5]. We synthesized Mo-SiN_x and Co-SiN_x GMs by co-sputtering Mo or Co with Si_3N_4. Scanning transmission electron microscopy (STEM) and conductivity measurements show the structural and electrical properties of the SiN_x-based GMs are comparable to the more commonly studied YSZ GMs [5]. X-ray photoemission spectroscopy (XPS) indicates that SiN_x GMs can exhibit metal-silicide and metal-nitride formations that limit the dielectric quality of the insulator. Despite these secondary phases, establishing SiN_x as a potential GM insulator material allows greater freedom to select metal-insulator combinations based on the reactivity of the chosen metal. Furthermore, while there are no clear ways to eliminate metal-oxide formation in GMs with oxide insulators, we propose several ways to mitigate secondary phase formation in SiN_x GMs.

Experimental details

We synthesized Mo-SiN_x and Co-SiN_x GM thin films, with $0.2 \leqslant \varphi \leqslant 0.8$, via radio frequency co-sputtering of 2-inch Mo, Co, and Si_3N_4 targets purchased from ACI alloys. As nitrogen vacancies occur in sputtered Si_3N_4 [27], we refer to the sputtered insulator as SiN_x. Depositions were performed in a high vacuum (HV) chamber with base pressure $<5 \times 10^{-7}$ Torr. The Si_3N_4 sputtering power was 100 W for $\varphi \leqslant 0.5$, and 50 W for $\varphi \geqslant 0.6$; metal sputtering powers were varied to achieve the desired φ. Individual SiN_x and metal deposition rates were measured from sample cross sections via scanning electron microscopy and used to calculate the GM volumetric metal fraction. The GM depositions took place in a 5 mTorr Ar atmosphere with 2.5–4.1 nm min^{-1} deposition rates.

For STEM measurements, 5 nm thick GM films were grown on 20 nm thick SiO_2 TEM windows. For XPS and van der Pauw (vdP) measurements, 100 nm thick GM films with a 10 nm SiN_x capping layer were grown on 10×10 mm^2 sapphire substrates. For vdP measurements, the samples were transferred to a separate HV chamber where a shadow mask defined 2×2 mm^2 corner electrode areas. Then 400 V Ar-ion milling with a KRI ion source was used to remove the SiN_x capping layer in the open regions of the shadow mask. The ion mill removal rate was calculated from SEM thickness measurements of SiN_x films before and after ion milling, and the milling time was chosen to penetrate ~2 nm below the capping layer and into the GM films. Then Ti/Au 10/100 nm electrodes were sputter deposited *in situ* through the shadow mask to create the 2×2 mm^2 corner electrodes. While the ion milling process may introduce compositional variations in the GM surface just below the electrical contacts, the SiN_x capping layer minimizes surface conduction and prevents oxidation of the surface metal nanoparticles, increasing measurement reliability. The conductivities reported are the average of vdP measurements in all four cardinal directions. The relatively large contact sizes aided cryogenic conductivity measurements, yet result in an ~5% error in vdP conductivity measurements [28]. While these variations are not insignificant, this paper focuses on orders-of-magnitude conductivity changes, and our conclusions are not affected by these comparatively small errors.

Photoemission measurements were performed using a Kratos Axis Supra XPS with a monochromatic Al K_α x-ray source. For XPS measurements, the SiN_x capping layer was removed with a gas cluster ion source, and samples were charge neutralized with an electron flood gun. The SiN_x XPS spectra prior to removing the capping layer were charge-corrected using the C 1s peak at 285 eV. After removing the surface carbon and SiN_x capping layer, the films were charge-corrected by comparing the Si, N, and O peaks in the GM films to the already charge-corrected Si, N, and O peaks from the SiN_x capping layer. The XPS analysis was performed in CASA XPS utilizing Kratos sensitivity factors, and peak fitting was done in the XPST extension of Igor Pro.

The STEM measurements were performed using an FEI Titan G2 80-200 microscope equipped with a spherical aberration corrector on the probe-forming optics. STEM images were analyzed with a combination of MATLAB's image processing algorithms and NIH's ImageJ [29]. The nanoparticle diameters were calculated from the individual (non-overlapping) areas, assuming circular nanoparticles. A Keithley 2450 source measurement unit was used for room temperature vdP measurements, and an accent optical technologies Hall effect measurement system, HL5500PC, was used for electrical measurements at 75 K.

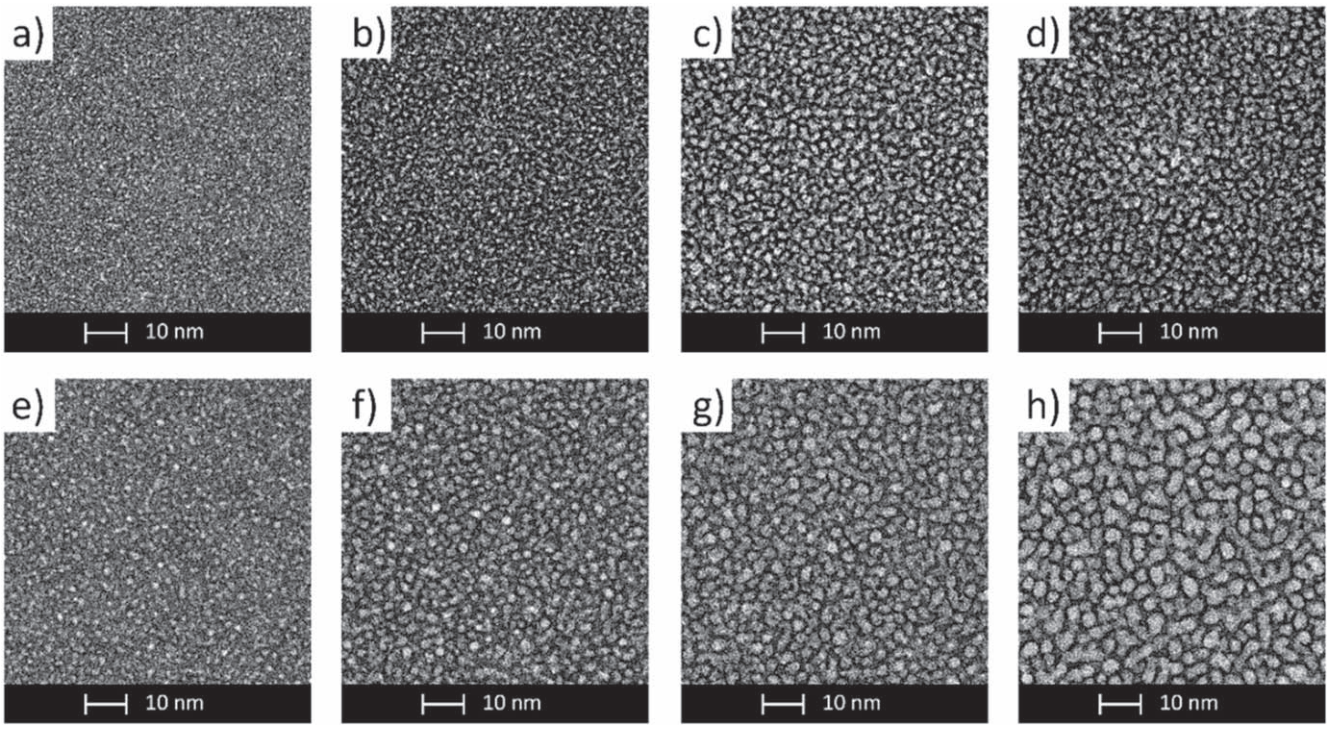

Figure 1. HAADF STEM images of 5 nm thick Mo-SiN_x (a)–(d) and Co-SiN_x (e)–(h) with $\varphi = 0.2$ (a), (e), $\varphi = 0.3$ (b), (f), $\varphi = 0.4$ (c), (g), and $\varphi = 0.5$ (d), (h).

Results and discussion

As anticipated, co-sputtering Mo or Co with Si_3N_4 results in the desired GM nanostructure with predominantly 1–3 nm diameter metal nanoparticles, as seen in the high-angle annular dark-field (HAADF) STEM images in figure 1. In the $\varphi = 0.4$–0.5 samples, significant overlapping of the metal nanoparticles is observed in both Mo-SiN_x and Co-SiN_x. The nanoparticle diameter distributions for $0.2 \leqslant \varphi \leqslant 0.5$ are reported in figure S1 of the supplementary information. Nanoparticle sizes scale with φ, and Co nanoparticles are larger than Mo nanoparticles for the same φ. The Co and Mo nanoparticle diameters are comparable to those in Mo-YSZ and Co-YSZ [5], suggesting the metal has a greater influence on nanoparticle diameters than the insulator. As noted previously [5], the nanoparticle diameter differences between Co and Mo are likely due to the different thermal stabilities of the metals; the melting temperatures of Co and Mo are 1495 °C and 2600 °C, respectively.

The Mo-SiN_x and Co-SiN_x conductivities exhibit the φ dependence intrinsic to GMs. Figure 2 shows a desirable rapid decline for Mo-SiN_x conductivity below φ_c, reaching 4×10^{-4} S cm^{-1} at $\varphi = 0.2$, implying that conduction is dominated by electron tunneling and strongly dependent on φ. Conversely, Co-SiN_x conductivity decays gradually with 3×10^{-1} S cm^{-1} at $\varphi = 0.2$, indicating defect-dominated transport within the insulator. This 3 orders-of-magnitude conductivity difference between Mo-SiN_x and Co-SiN_x is not seen in Mo-YSZ and Co-YSZ where conductivity is 7×10^{-2} and 1×10^{-2} S cm^{-1}, respectively, at $\varphi = 0.2$ [5].

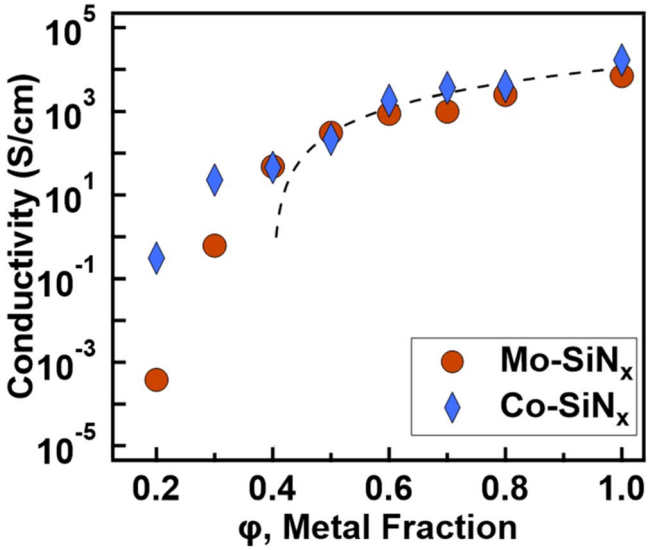

Figure 2. The vdP conductivity as a function of the volumetric metal fraction for Mo-SiN_x and Co-SiN_x GM thin films. The dotted line is a fit to equation (1) of the averaged Mo-SiN_x and Co-SiN_x conductivities.

The σ versus φ plots in figure 2 were fit according to the percolation power-law, equation (1), which applies for $\varphi > \varphi_c$ [30]. For three-dimensional percolation networks, $t = 2$. From analysis of the STEM images in figure 1 and temperature dependent conductivity measurements (figure S2 in the supplementary information), we estimate $\varphi_c = 0.4$. While this percolation threshold is only a rough estimate, it guided our selection of $\varphi = 0.3$ as representative insulating-regime GMs

for XPS studies.

$$\sigma \propto (\varphi - \varphi_c)^t. \quad (1)$$

The divergence in conductivity trends between Mo-SiN_x and Co-SiN_x at low φ implies different concentrations of secondary phases (metal-nitrides and metal-silicides) within these GMs. When $\varphi < \varphi_c$, σ depends on both the separation distance between metal nanoparticles and the formation of the metal-insulator secondary phases. Smaller nanoparticle diameters, with constant φ, result in shorter separation distances [4, 31] promoting tunneling conduction between the nanoparticles and increasing σ. However, Co nanoparticles are larger diameter than Mo nanoparticles (figure S1), yet Co-SiN_x's σ is significantly higher for $\varphi < \varphi_c$. Purely considering the GM nanostructure, Co-SiN_x is expected to be less conductive than Mo-SiN_x, opposite of the conductivity trends observed in figure 2. As geometric differences alone cannot explain the large variance in conductivity between the Mo-SiN_x and Co-SiN_x GMs when $\varphi < \varphi_c$, different levels of secondary phase formation are likely. Secondary phase formations increase the insulator conductivity, particularly at low φ [5].

Based on XPS measurements, shown in figure 3, metal-silicide is present in Mo-SiN_x and Co-SiN_x. The Si 2p XPS spectra for sputtered SiN_x has a single peak centered at 102.2 eV, consistent with either SiN_x or Si_3N_4 [32–34]. In both Mo-SiN_x (figure 3(a)) and Co-SiN_x, a secondary Si 2p XPS peak exists at 99.3–99.4 eV, consistent with $MoSi_2$ [35] or $CoSi_2$ [36] formation. While the Si 2p binding energy in pure Si is also 99.3 [37] pure Si clusters within the GMs are unlikely given the enthalpies of nitrides and silicides, which will be discussed later. For Co-SiN_x, the Si 2s XPS peak (figure 3(b)) was also measured as the overlap between the Co 3s and Si 2p XPS peaks obscures Co-silicide analysis. Like the Si 2p spectra, the Si 2s spectra show a primary peak at 153.4 eV and a secondary Co-silicide peak with 2.8 eV lower binding energy.

We attribute metal-silicide formation to nitrogen vacancies in the sputtered Si_3N_4 [27]; without sufficient nitrogen, Si bonds with either Mo or Co instead. The percentage of Si atoms forming Co-silicide remains relatively constant at all metal fractions (figure 3(c)). However, the Mo-silicide formation in the Mo-SiN_x scales with φ. These percentages are determined by taking the area of the lower binding energy peaks in figures 3(a) and (b) and dividing by the total area of the Si 2p or Si 2s peaks. In Mo-SiN_x, the greater levels of Mo-silicide at higher Mo concentrations can be explained by Mo-nitride formation, which increases the vacancy fraction in the SiN_x.

Mo-nitride formation is indicated by the binding energy shift of the N 1s XPS peak (figure 4). For the sputtered SiN_x films, the N 1s peak occurs at 398.0 eV, see figure S3 in the supplementary information. In Mo-SiN_x with $\varphi = 0.2$, the N 1s binding energy remains at 398.0 eV indicating that most of the nitrogen remains bound to Si. However, as φ increases the N 1s binding energy decreases and stabilizes at ~397.5 eV for $\varphi \geqslant 0.5$, which is consistent with the binding energy of Mo_2N [38]. This binding energy shift suggests that for $\varphi \geqslant 0.5$ a significant portion of the nitrogen is bound to Mo rather than Si. As more nitrogen is removed from the SiN_x, more Si becomes available to form Mo-silicide (figure 3(c)). In Co-SiN_x, the near constant N 1s binding energy (figure 4) and Co-silicide levels (figure 3(c)) both suggest Co-nitrides do not form.

The GM conductivity above φ_c follows the percolation power law (equation (1)), as expected for a disordered metal. The conductivity drop from $\varphi = 1.0$ (pure metals) to $\varphi = 0.6$ is ~1 order-of-magnitude for both Co-SiN_x and Mo-SiN_x, figure 2. These conductivity changes are comparable to noble metal GMs [4] suggesting that the metal nanoparticle conductivities are not significantly reduced by metal-silicide and metal-nitride formation. Unlike the N 1s and Si 2p peaks, the only indication of secondary components seen in the Co 2p and Mo 3p XPS spectra is a peak broadening that is more pronounced at low φ, see figure S4 in the supplementary information. For Co-SiN_x with $\varphi = 0.2$, the FWHM of the Co 2p peak is 25% larger than for pure Co. In Mo-SiN_x, the broadening is further enhanced with the Mo 3d FWHM increasing by 100% in the $\varphi = 0.2$ sample compared to pure Mo. This peak broadening indicates heterogeneity in the metal binding environments and may be caused by metal-nitrides [38, 39] and metal-silicides [35, 36] that have similar binding energies to the pure metals [37]. However, the Co 2p and Mo 3d XPS spectra cannot quantify the extent of metal-silicide or metal-nitride formation.

The metal-insulator secondary phases inferred from XPS components in figures 3 and 4 are consistent with the relative thermodynamic stabilities of metal-silicides and metal-nitrides, summarized in table 1. Co-silicides, Mo-silicides, and Mo-nitrides have enthalpies in the range of −95 to −314 kJ^*mol^{-1}. While these enthalpies are less negative than the enthalpy for Si_3N_4, they are sufficient to form measurable metal-silicide and Mo-nitride levels, as inferred by XPS analysis (figures 3 and 4). Conversely, the enthalpies for Co-nitrides are close to zero, and there is no evidence of Co-nitride formation in the Co-SiN_x GMs. While the enthalpies of these compounds reasonably explain the phases present within the GMs, the enthalpies do not provide a reason for the higher amounts of Co-silicide compared to Mo-silicide in the $\varphi = 0.2$–0.3 GMs, figure 3(c).

The relative atomic volumes for Co and Mo contribute to the metal-silicide levels at low φ. At $\varphi = 0.2$, there is minimal metal-nitride formation, figure 4, so the number of nitrogen vacancies in the SiN_x should be comparable for both Mo-SiN_x and Co-SiN_x. However, based on the atomic volumes of Co (6.7 $cm^3\ mol^{-1}$) and Mo (9.4 $cm^3\ mol^{-1}$), there will be ~40% more Co atoms than Mo atoms at the same volumetric metal fraction. If the availability of Si is equal in Mo-SiN_x and Co-SiN_x, the larger amount of Co reactants will result in higher levels of Co-silicides, consistent with the observations in figure 3(c). In the Co-SiN_x, the available Si to form Co-silicide is limited to the typical nitrogen vacancies found in sputtered Si_3N_4 [27]; however, at higher metal fractions the larger amount of Co reactants should still result in higher Co-silicide levels. The Co-SiN_x linear fit in figure 3(c) shows minimal φ dependence. The comparable Co-silicide levels at

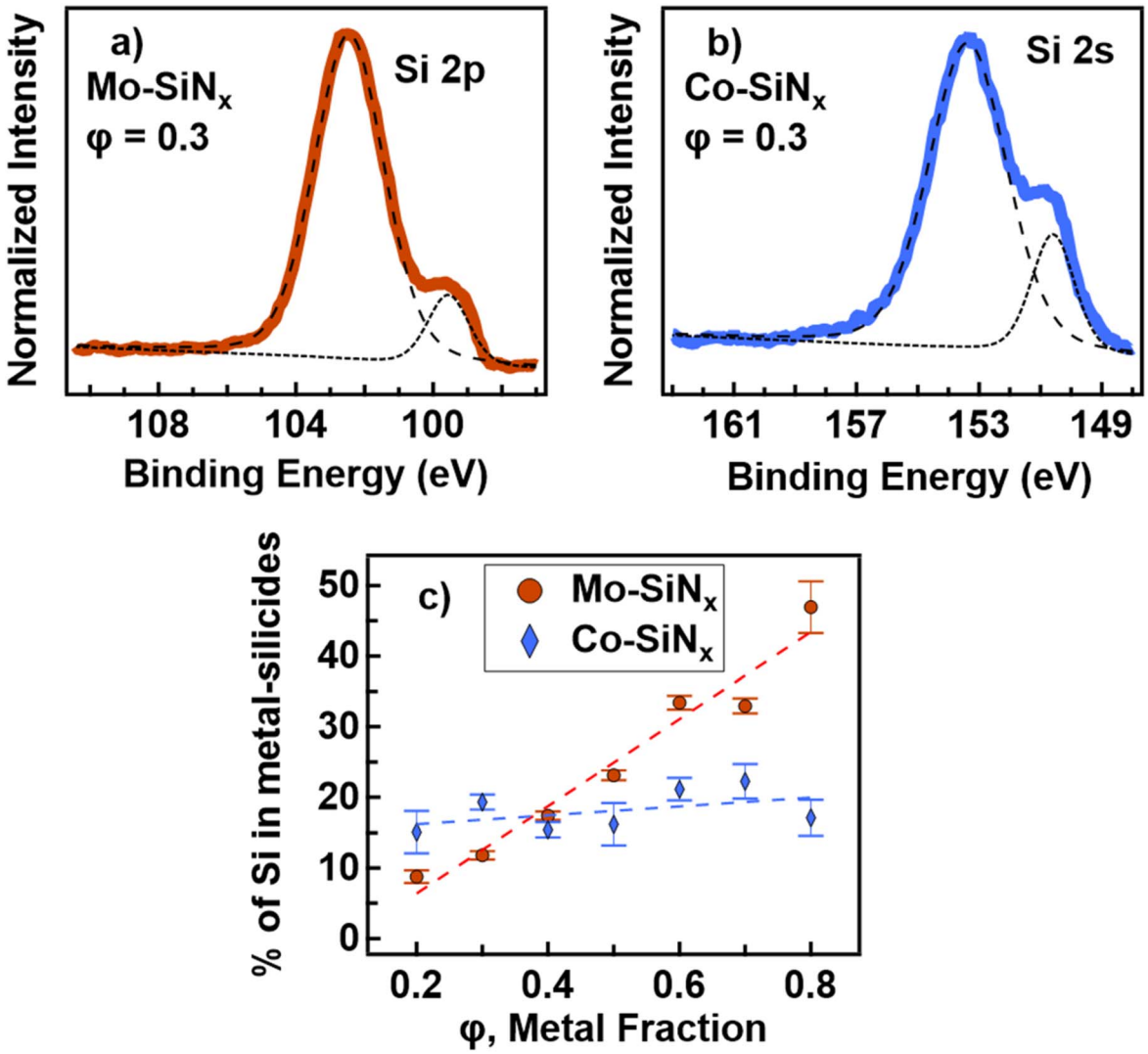

Figure 3. (a) The Si 2p XPS spectra for Mo-SiN$_x$ with $\varphi = 0.3$. (b) The Si 2s XPS spectra for Co-SiN$_x$ with $\varphi = 0.3$. In (a) and (b) the red/blue solid lines are the experimental data and black dotted lines are the results of peak fitting. (c) The percentage of Si atoms forming metal-silicides in Mo-SiN$_x$ and Co-SiN$_x$ for varying metal fractions based on the area ratios of Si peaks seen in (a) and (b). In (c), the dotted lines are linear fits of the data, and the error bars are based on peak fitting Monte Carlo simulations performed in CasaXPS.

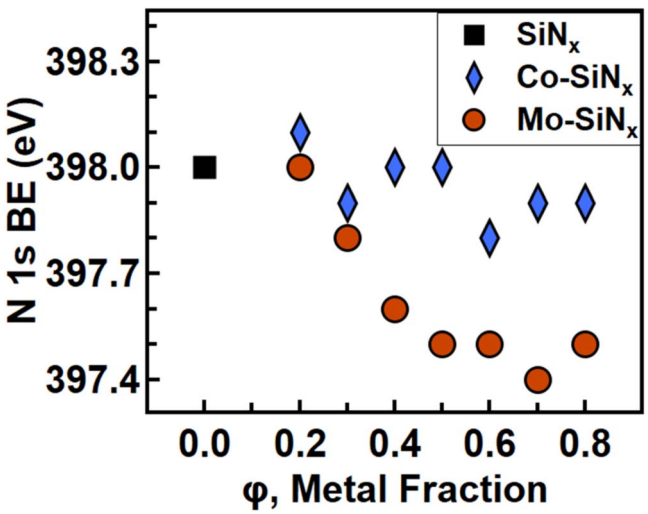

Figure 4. The binding energy (BE) of the N 1s XPS peak in Mo-SiN$_x$ and Co-SiN$_x$ for varying metal fractions.

all metal fractions suggests that the majority of available Si is already forming Co-silicide at low φ, so the Co-silicide content cannot appreciably increase.

We reconsider the conductivity trends reported in figure 2 in light of these secondary phases. Above φ_c, the metal-silicide and metal-nitride formation have minimal effect on the GM conductivity, but below φ_c, these secondary phases can dramatically alter σ, as illustrated by the divergence of Mo-SiN$_x$ and Co-SiN$_x$ conductivity at low φ. The conductivities of bulk Mo-silicides, Co-silicides, and Mo-nitrides are 1–5 $\times$ 10^4 S cm^{-1} [46, 47] while bulk Mo and Co conductivities are $\sim$2 $\times$ 10^5 S cm^{-1} [48]. For $\varphi > \varphi_c$, conduction occurs primarily through a percolating metal network; while electron tunneling may still occur, the insulator quality plays a lesser role in the GM conductivity in this regime. For $\varphi < \varphi_c$, metal-silicides and Mo-nitrides will increase the GM conductivity. The higher Co-silicide levels compared to Mo-silicide (figure 3(c)) likely contribute to the 3

Table 1. A summary of the enthalpies of formation for possible compounds in the Mo-SiN_x and Co-SiN_x GMs.

Group	Compound	$\Delta_f H$ (kJ*mol^{-1})	References
Silicon nitride	Si_3N_4	−828	[24]
Mo-silicides	Mo_3Si	−125	[40]
	Mo_5Si_3	−314	[41]
	$MoSi_2$	−137	[42]
Co-silicides	Co_2Si	−123	[43]
	CoSi	−95	[43]
	$CoSi_2$	−99	[43]
Mo-nitrides	Mo_2N	−123	[44]
	MoN	−102	[44]
Co-nitrides	Co_4N	+14	[45]
	Co_2N	−27	[44]
	CoN	0	[44]

order-of-magnitude conductivity difference between Co-SiN_x and Mo-SiN_x at $\varphi = 0.2$ (figure 2).

There are three possible locations for the metal-silicide and metal-nitride formation: within the insulator, within the metal nanoparticles, or at the metal-insulator interface. While the precise location of these formations cannot be determined by the measurements reported here, the primary effect of secondary phases on GM conductivity is an increase in defect-mediated electron tunneling. Secondary phases within the SiN_x insulating matrix will increase defect-mediated electron tunneling by providing additional electron tunneling paths. Secondary phases within the metal nanoparticles or at the metal-insulator interface will result in insulator vacancies, as seen for Mo-YSZ and Co-YSZ [5]. Therefore, the increased conductivity at low φ is mainly attributed to an increase in defect-mediated electron tunneling, which may be caused by either secondary phase formations within the insulator or insulator vacancies.

We posit that the desirable low conductivity below φ_c for Mo-SiN_x GMs demonstrates the suitability of silicon nitride as a GM insulator. This low conductivity suggests transport in Mo-SiN_x GMs is dominated by thermally-assisted electron-tunneling and that Mo-SiN_x GMs have fewer insulator defects compared to other non-noble metal GMs. The 4×10^{-4} S cm^{-1} for Mo-SiN_x at $\varphi = 0.2$ is among the lowest conductivities reported for Co-, Fe-, Ni- and W-based GMs [15]. In Mo-SiN_x, the prevalence of secondary phases decreases with decreasing φ; and at $\varphi = 0.2$, Mo-SiN_x is 2–3 orders-of-magnitude less conductive than Co-SiN_x, Co-YSZ [5], and Mo-YSZ [5]. Controlling secondary phase formation in SiN_x-based GMs will be crucial for achieving GMs with pristine insulators, as it is for GMs containing oxide insulators [5, 49, 50].

Several potential methods to improve SiN_x-based GMs exist that may not be possible for oxide-insulators. The metal-silicide formation seen in Co-SiN_x is caused by nitrogen vacancies in the sputtered Si_3N_4, which may be mitigated by either growing or annealing the Co-SiN_x in a partial N_2 environment. Sputtering Si_3N_4 in a partial N_2 environment reduces the nitrogen vacancies and can increase the resistivity of the insulator by 4 orders-of-magnitude [27]. Sputtering metals in a N_2 environment can also result in metal-nitrides [51], which would be detrimental for GMs if the metal-nitride formation significantly decreased the conductivity of the metal nanoparticles. However, many Co-nitrides are metallic [52] and therefore Co-nitride formation may be an acceptable consequence of sputtering in N_2 if the SiN_x insulating quality is significantly improved. As such, highly resistive Co-Si_3N_4 GMs may be possible under the correct growth conditions. Further study is underway.

Silicon nitride could also be used to create other nanostructured materials with metal-nitride nanoparticles, even when the metal-nitrides are non-metallic. Metal-nitride nanostructures have a variety of potential applications in plasmonics [53], optics [54], catalysis [55], sensing [56], and energy storage [57]. For example, transition metal nitride nanoparticles exhibit localized surface plasmon resonance in the visible and near infrared range [53] which could be used for biosensing [58] and optical cloaking [59]. Therefore, the insights gained from the Co-SiN_x and Mo-SiN_x GMs in this study provide a means for developing a family of nanostructured SiN_x materials for numerous applications.

Conclusion

We showed that SiN_x-based GMs can be synthesized by co-sputtering Si_3N_4 with Mo or Co. These GMs constitute an exemplar material system for interfacial engineering studies. Mo-SiN_x, a promising high thermal-stability GM, has the desired low conductivity below the percolation threshold. The SiN_x GM nanostructures are comparable to other GMs with non-noble transition metals and oxide insulators. Deleterious metal-nitride and metal-silicide secondary phases were identified through XPS analysis. At low metal fractions, there is minimal secondary phase formation in high thermal stability Mo-SiN_x, importantly reducing defect-mediated electron tunneling. Thermodynamic considerations suggest increasing Co-SiN_x nitrogenation will reduce defects in Co-SiN_x GMs. Future work will focus on further reducing these insulator defects and secondary phase formations in SiN_x systems for highly insulating GMs or utilizing secondary phase formation to create metal-nitride nanostructured materials. Overall, we find that SiN_x-based GMs provide new material pathways to advance the utility of nanogranular systems.

Acknowledgments

The authors thank L Brunke, W Bachman, and P Sharma for technical assistance with the sample preparation, electrical measurements, and helpful discussions, respectively. This work was supported by the Laboratory Directed Research and Development (LDRD) program at Sandia National Laboratories. Sandia National Laboratories is a multimission laboratory managed and operated by National Technology and Engineering Solutions of Sandia, LLC (NTESS), a wholly owned subsidiary of Honeywell International Inc., for

the US Department of Energy's National Nuclear Security Administration under contract DE-NA0003525. This written work is authored by an employee of NTESS. The employee, not NTESS, owns the right, title and interest in and to the written work and is responsible for its contents. Any subjective views or opinions that might be expressed in the written work do not necessarily represent the views of the US Government. The publisher acknowledges that the US Government retains a non-exclusive, paid-up, irrevocable, worldwide license to publish or reproduce the published form of this written work or allow others to do so, for US Government purposes. The DOE will provide public access to results of federally sponsored research in accordance with the DOE Public Access Plan.

Data availability statement

All data that support the findings of this study are included within the article (and any supplementary files).

Conflict of interest

The authors have no conflicts to disclose.

ORCID iDs

Simeon J Gilbert https://orcid.org/0000-0003-0402-9305
Melissa L Meyerson https://orcid.org/0000-0001-9327-442X
Paul G Kotula https://orcid.org/0000-0002-7521-2759
Samantha G Rosenberg https://orcid.org/0000-0001-5033-5675
Michael P McGarry https://orcid.org/0000-0003-3135-4306
Laura B Biedermann https://orcid.org/0000-0001-5293-9034

References

[1] Hattink B J, Labarta A, García del Muro M, Batlle X, Sánchez F and Varela M 2003 *Phys. Rev.* **67** 033402
[2] García del Muro M, Konstantinović Z, Batlle X and Labarta A 2013 *J. Phys. D: Appl. Phys.* **46** 495304
[3] Bakkali H, Dominguez M, Batlle X and Labarta A 2015 *J. Phys. D: Appl. Phys.* **48** 335306
[4] Grimaldi C 2014 *Phys. Rev.* **89** 214201
[5] Gilbert S J, Rosenberg S G, Kotula P G, Kmieciak T G, Biedermann L B and Siegal M P 2022 *J. Phys.: Condens. Matter* **34** 204007
[6] Jonscher A K 1977 *Nature* **267** 673–9
[7] Jonscher A K 1999 *J. Phys. D: Appl. Phys.* **32** R57–70
[8] Bakkali H, Dominguez M, Batlle X and Labarta A 2016 *Sci. Rep.* **6** 29676
[9] Bakkali H, Blanco E, Lofland S E and Domínguez M 2020 *New J. Phys.* **22** 083018
[10] Bakkali H and Dominguez M 2013 *Europhys. Lett.* **104** 17007
[11] Mitani S, Takahashi S, Takanashi K, Yakushiji K, Maekawa S and Fujimori H 1998 *Phys. Rev. Lett.* **81** 2799–802
[12] Miller N C and Shirn G A 1967 *Appl. Phys. Lett.* **10** 86–8
[13] Abeles B, Sheng P, Coutts M D and Arie Y 1975 *Adv. Phys.* **24** 407–61
[14] Beloborodov I S, Lopatin A V, Vinokur V M and Efetov K B 2007 *Rev. Mod. Phys.* **79** 469–518
[15] Bakkali H, Blanco E, Dominguez M and Garitaonandia J S 2017 *Nanotechnology* **28** 335704
[16] McLean W L 1985 *Nature* **315** 372–372
[17] Rylkov V V *et al* 2018 *J. Magn. Magn. Mater.* **459** 197–201
[18] Cao Y, Kobayashi N, Wang C, Takahashi S, Maekawa S and Masumoto H 2023 *Adv. Electron. Mater.* **9** 2201218
[19] Schwebke S, Winter S, Koch M and Schultes G 2018 *J. Appl. Phys.* **124** 235308
[20] Schultes G, Schmid-Engel H, Schwebke S and Werner U 2018 *J. Sensors Sensor Syst.* **7** 1–11
[21] Hanefeld M, Gruszka P and Huth M 2021 *Sci. Rep.* **11** 15163
[22] Priestley E B, Abeles B and Cohen R W 1975 *Phys. Rev.* B **12** 2121–4
[23] Cohen R W, Cody G D, Coutts M D and Abeles B 1973 *Phys. Rev.* B **8** 3689–701
[24] O'Hare P A G, Tomaszkiewicz I, Beck I C M and Seifert H J 1999 *J. Chem. Thermodyn.* **31** 303–22
[25] Nag A, Rao R R and Panda P K 2021 *Ceram. Int.* **47** 20793–806
[26] Krstic Z and Krstic V D 2011 *J. Mater. Sci.* **47** 535–52
[27] Vila M, Prieto C and Ramírez, R 2004 *Thin Solid Films* **459** 195–9
[28] Chwang R, Smith B J and Crowell C R 1974 *Solid-State Electron.* **17** 1217–27
[29] Schneider C A, Rasband W S and Eliceiri K W 2012 NIH Image to ImageJ: 25 years of image analysis *Nature Methods* **9** 671
[30] Toker D, Azulay D, Shimoni N, Balberg I and Millo O 2003 *Phys. Rev.* **68** 041403(R) B
[31] Seager C H and Pike G E 1974 *Phys. Rev.* B **10** 1435–46
[32] Ghosh S K and Hatwar T K 1988 *Thin Solid Films* **166** 359–66
[33] Sekine K, Saito Y, Hirayama M and Ohmi T 2000 *IEEE Trans. Electron Devices* **47** 1370–4
[34] Ku S-L and Lee C-C 2010 *Opt. Mater.* **32** 956–60
[35] Rastogi R S, Vankar V D and Chopra K L 1992 *J. Vac. Sci. Technol.* A **10** 2822–5
[36] Bernal-Ramos K, Saly M J, Kanjolia R K and Chabal Y J 2015 *Chem. Mater.* **27** 4943–9
[37] Moulder J F, Stickle W F, Sobol P E and Bomben K D 1992 *Handbook of X-Ray Photoelectron Spectroscopy: A Reference Book of Standard Spectra for Identification and Interpretation of XPS Data* (Eden Prairie, Minnesota: Physical Electronics Division, Perkin-Elmer Corp.)
[38] Sanjinés R, Wiemer C, Almeida J and Lévy F 1996 *Thin Solid Films* **290-291** 334–8
[39] Cruz W D L, Contreras O E, Soto G and Pérez-Tijerina E 2006 *Rev. Mex. Fis.* **52** 409–12
[40] Tomaszkiewicz I, Hope G A, Beck Ii C M and O'Hare P A G 1996 *J. Chem. Thermodyn.* **28** 29–42
[41] Tomaszkiewicz I, Hope G A, Beck Ii C M and O'Hare P A G 1997 *J. Chem. Thermodyn.* **29** 87–98
[42] O'Hare P A G 1993 *J. Chem. Thermodyn.* **25** 1333–43
[43] Lexa D, Kematick R J and Myers C E 1996 *Chem. Mater.* **8** 2636–42
[44] Niessen A K and De Boer F R 1981 *J. Less-Common Met.* **82** 75–80
[45] Milad I K, Smith K J, Wong P C and Mitchell K A R 1998 *Catal. Lett.* **52** 113–9
[46] Murarka S P 1983 *Silicides for Vlsi Applications* ed S P Murarka (San Diego: Academic) pp 29–70

[47] Jauberteau I, Bessaudou A, Mayet R, Cornette J, Jauberteau J, Carles P and Merle-Méjean T 2015 *Coatings* **5** 656–87
[48] Lide D R 1992 *CRC Handbook of Chemistry and Physics* 73 edn (Boca Raton, FL: CRC Press)
[49] Shah S I, Doele B A, Weerasekera I and Unruh K M 1991 *Thin Solid Films* **206** 264–8
[50] Paparazzo E, Dormann J L and Fiorani D 1983 *Phys. Rev.* B **28** 1154–7
[51] Oda K, Yoshio T and Oda K 1987 *J. Mater. Sci.* **22** 2729–33
[52] Chen P, Xu K, Tong Y, Li X, Tao S, Fang Z, Chu W, Wu X and Wu C 2016 *Inorg. Chem. Frontiers* **3** 236–42
[53] Gutiérrez Y, Brown A S, Moreno F and Losurdo M 2020 *J. Appl. Phys.* **128** 080901
[54] Xie R-J, Bert Hintzen H T and Johnson D 2013 *J. Am. Ceram. Soc.* **96** 665–87
[55] Rasaki S A, Zhang B, Anbalgam K, Thomas T and Yang M 2018 *Prog. Solid State Chem.* **50** 1–15
[56] Shafiee S A, Perry S C, Hamzah H H, Mahat M M, Al-lolage F A and Ramli M Z 2020 *Electrochem. Commun.* **120** 106828
[57] Ashraf I, Rizwan S and Iqbal M 2020 *Frontiers Mater.* **7** 181
[58] Petryayeva E and Krull U J 2011 *Anal. Chim. Acta* **706** 8–24
[59] Alù A and Engheta N 2008 *J. Opt. A: Pure Appl. Opt.* **10** 093002